



Long-term array observation by ocean bottom seismometers at the Chile Triple Junction



Aki Ito ^{a,*}, Hajime Shiobara ^b, Matthew Miller ^c, Hiroko Sugioka ^d, Javier Ojeda ^{e,f}, Carlos Tassara ^{c,g}, Masanao Shinohara ^b, Masataka Kinoshita ^b, Hikaru Iwamori ^b

^a Japan Agency of Marine-Earth Science and Technology, 2-15 Natsushima-cho, Yokosuka, Kanagawa, 237-0061, Japan

^b Earthquake Research Institute, University of Tokyo, 1-1-1, Yayoi, Bunkyo-ku, Tokyo, 113-0032, Japan

^c Department of Geophysics, University of Concepción, Casilla, 160-C, Concepción, Chile

^d Ocean-Bottom Exploration Center, Kobe University, 5-1-1, Fukae Minami-cho, Higashi Nada-ku, Kobe, Hyogo, 658-0022, Japan

^e Departamento de Geofísica, Universidad de Chile, Av. Blanco Encalada, 2002, Santiago, Chile

^f Université Paris Cité, Institut de Physique Du Globe de Paris, CNRS, F-75005, Paris, France

^g Faculty of Science, Arturo Prat University, Arturo Prat, 2120, Iquique, Chile

ARTICLE INFO

Keywords:

Chile
Triple junction
Subduction
Ocean bottom seismometer
Broadband seismic observation

ABSTRACT

Seafloor seismic observations were conducted twice in the vicinity of the Chile Triple Junction (CTJ) in order to investigate the crustal activities associated with the subduction of the hot ridge. Herein, we present the details of the most recent seismic observation for the two-year period between January 2019 and January 2021. Furthermore, the hypocenter location, magnitude, and focal mechanisms of the local earthquakes were revealed by analyzing the data from both deployments, including the one conducted between 2009 and 2010. In total, more than 2100 local earthquakes were detected during the two observation periods. In both observations, earthquakes were found to have actively occurred along the Chile Ridge and the Darwin Fracture Zone. The magnitudes of these earthquakes range from -0.3 to 5.0. From the events cataloged during the time period 2019 to 2021, a clear seismicity gap is observed at 46.4°S with the predominant faulting type differing across this divide. North of the seismicity gap, normal faulting earthquakes periodically occur along the Chile Ridge, thereby indicating continuous ridge opening. By contrast, the earthquakes to the south of the seismicity gap, where the Chile Ridge has already been subducted, occurred intermittently and are dominated by reverse faulting. The latter earthquakes are associated with the Antarctic plate subduction. We propose that a local transform fault, with E-W strike direction, exists 10 km north of the seismicity gap, based on the hypocenter locations and focal mechanisms of three M > 4 earthquakes. This local transform fault was probably formed by the effect of the active ridge subduction.

© 2017 Elsevier Inc. All rights reserved.

1. Introduction

The Chile Triple Junction (CTJ) is located off the southern coast of Chile at a latitude of around 46.0–46.5°S, where the active spreading ridge between the Nazca Plate and Antarctic Plate collides with the Chile Trench and is subducting below the South American Plate (e.g., Cande and Leslie, 1986; Tebbens et al., 1997; Lagabrielle et al., 2000; Lagabrielle et al., 2015) (Fig. 1). The current half spreading rate of the Chile Ridge is 26.5 mm/yr (Tebbens et al., 1997). This area is close to the southern end of the 1960 Chile earthquake fault zone (Gran Terremoto de Valdivia) and is slightly outside the huge tsunami source region (e.g.,

Barrientos and Ward, 1990; Moreno et al., 2009). In the vicinity of the CTJ, active non-volcanic tremors have been reported (e.g., Ide, 2012; Gallego et al., 2013) based on on-land observations. These phenomena seem to be related to subduction of the hot ridge and newly-generated oceanic floor, possibly affecting the continental side by adding heat and fluids derived from the subducting ridge and plates. Such thermal and fluid effects of the subducted ridge have been argued to be important also for the geological and tectonic evolution of the continent, associated with northward migration of the CTJ over the past 14 million years (Cande and Leslie, 1986; Iwamori, 2000; Breitsprecher and Thorkelson, 2009). An investigation of the seismicity and seismic

* Corresponding author.

E-mail address: iaki@jamstec.go.jp (A. Ito).

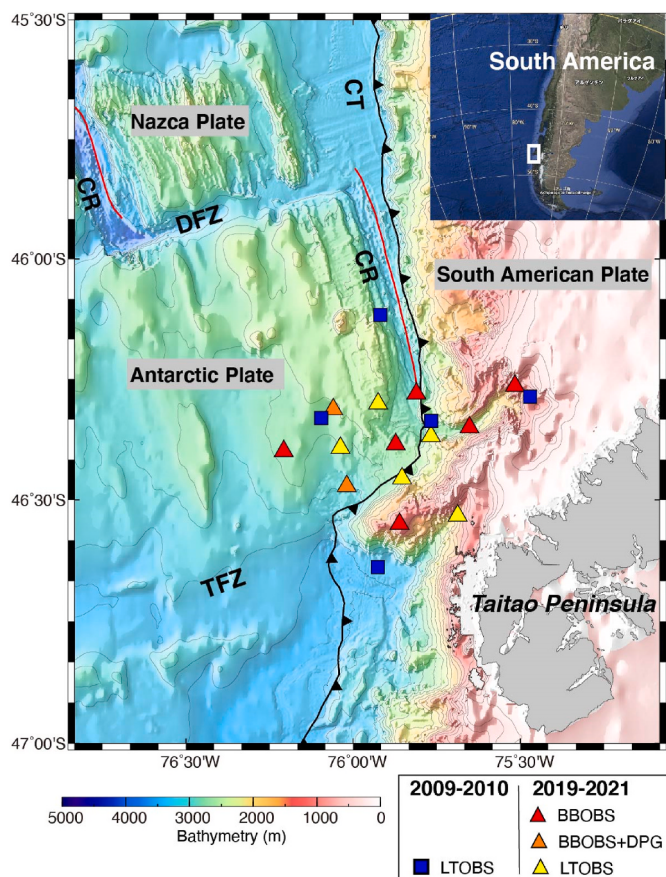


Fig. 1. The tectonic setting map showing the locations of the OBSs deployed in 2009–2010 (blue squares) and 2019–2021 (red, orange, and yellow triangles); CT = Chile Trench; CR = Chile Ridge; DFZ = Darwin fracture zone; TFZ = Taitao fracture zone. The red line and the black line with triangles indicate the locations of the Chile Ridge and the Chile Trench, respectively.

structure around the CTJ is therefore important in order to examine these thermal and fluid effects, and to address the long-standing geophysical problem of how the plate is generated at the spreading center, e.g., examining a plate model with a constant thickness (McKenzie, 1967) or with thermal thickening (Parker and Oldenburg, 1973).

Observations and surveys using ocean bottom seismometers are essential for investigating the seismicity and seismic structure in the offshore area. For instance, offshore studies have been extensively conducted using refraction surveys to image the shallow sedimentary and crustal structures from the northern to southern Chilean subduction zones (e.g., Scherwath et al., 2009; Contreras-Reyes et al., 2007, 2012; Maksymowicz et al., 2012). In addition, several ocean-bottom studies have been performed to examine the regional seismic activities and structures from shallow to mantle depths in the northern and central Chile subduction zones (Husen et al., 1999, 2000; Lange et al. 2007; Tilmann et al., 2008; Haberland et al., 2009; Hicks et al., 2014). Although no offshore seismic observations were performed in the close vicinity of the CTJ prior to 2009, the present research group conducted the very first such ocean bottom observation in this vicinity using five long-term ocean bottom seismometers (LTOBSs) with a 1-Hz sensor for one year, between March 2009 and February 2010. From this array observation, several micro-seismic activities along the Chile Ridge and the Darwin Fracture Zone (DFZ) (Shinohara et al., 2010), and non-volcanic tremors (Sáez et al., 2019), have been detected. These results could not have been obtained without the OBS data due to the sparsity of land seismic stations in this region, where only a few events have been detected by the Preliminary Determination of Epicenters

(PDE) catalog of the U.S. Geological Survey (USGS) over several years.

To investigate the same area over a broader frequency range, with more precise hypocenters and a longer observation period, we used 13 OBSs, including 8 broadband ocean bottom seismometers (BBOBSs), to perform a second OBS array observation for two years between January 2019 and January 2021. Whereas the first observation used a site spacing of more than 20 km, the spacing for the second observation was set at about 10 km in order to improve the accuracy of the depth determination, as it had been already shown that most of the small earthquakes near the CTJ have occurred at depths shallower than around 10 km (Shinohara et al., 2010). In addition, to investigate the crust/mantle structure, the OBS array for the second observation was designed to enable the following analyses: (i) the change in the crustal structure with increasing age from the ridge to the westward area, in order to examine a plate model, (ii) the structure from the crust to the upper mantle beneath the OBS array, as revealed by receiver functions, in order to understand the oceanic plate being subducted, and (iii) the mantle structure beneath the continental side affected by heat and fluids derived from the subducting ridge and plates. The BBOBS data off Chile will also be useful for improving the resolution of the global surface wave tomography (Isse et al., 2019).

The present paper introduces the second OBS array observation from January 2019 to January 2021 in detail, along with its first result of more than 2000 hypocenters originally detected from the OBS data. The hypocenter locations, earthquake magnitudes, and focal mechanisms of local earthquakes were determined, and the results for three $M > 4$ earthquakes occurring near the CTJ on December 26, 2020 were compared with those obtained from global data (i.e., the PDE and the Global Centroid-Moment-Tensor Project (GCMT) catalogues). In addition, the data from the first OBS observation was reanalyzed using the same procedure as for the second OBS data. The hypocenter locations and magnitudes of more than 100 earthquakes during March 2009 and February 2010 are presented herein.

2. Observation and data

2.1. Instruments and observation

External views of the BBOBSs and LTOBSs that were used in the second observation, are presented in Fig. 2a and b, respectively (Shinohara et al., 2012). BBOBS consists of a broadband seismic sensor (CMG-3T 360s for OBS, Guralp systems Ltd.) equipped with an original active leveling unit (Suetsugu and Shiobara, 2014). LTOBS was equipped with a 1 Hz seismic sensor (LE-3Dlite, Lennartz electronics GmbH). In each system, a data recorder, acoustic transponder, and lithium batteries were installed inside the titanium alloy sphere housing (diameter = 650 mm for the BBOBS, and 500 mm for the LTOBS). Each OBS was designed for free-fall deployment from the sea surface, and subsequent recovery from the sea floor was facilitated by self pop-up due to forced electrolytic corrosion of thin titanium plates that rigidly connected between the titanium sphere housing (remaining ~10 kgf of buoyancy) and the anchor (80 kgw). The forced electrolytic corrosion was initiated by a release command signal from the acoustic transponder. In the second observation, two of the BBOBSs were equipped with a differential pressure gauge (DPG; Araki and Sugioka, 2009), and six of the BBOBSs recorded 3-component mass position (acceleration) signals (Shiobara et al., 2021) to provide further geophysical information in addition to the standard ground velocity signals. The sampling frequency of the data recorders of all OBSs was set at 100 Hz, with 24 bits resolution to record the three component signals of the sensor.

The 8 BBOBSs and 5 LTOBSs used in the second observation were deployed around the center of the CTJ region at approximately 10 km intervals between the land slope of the trench in the east and the ocean floor in the west, as shown in Fig. 2c. The locations and functional data of these OBSs are summarized in Table S1. The deployment of the OBSs was conducted from January 17 to January 20, 2019 as part of the

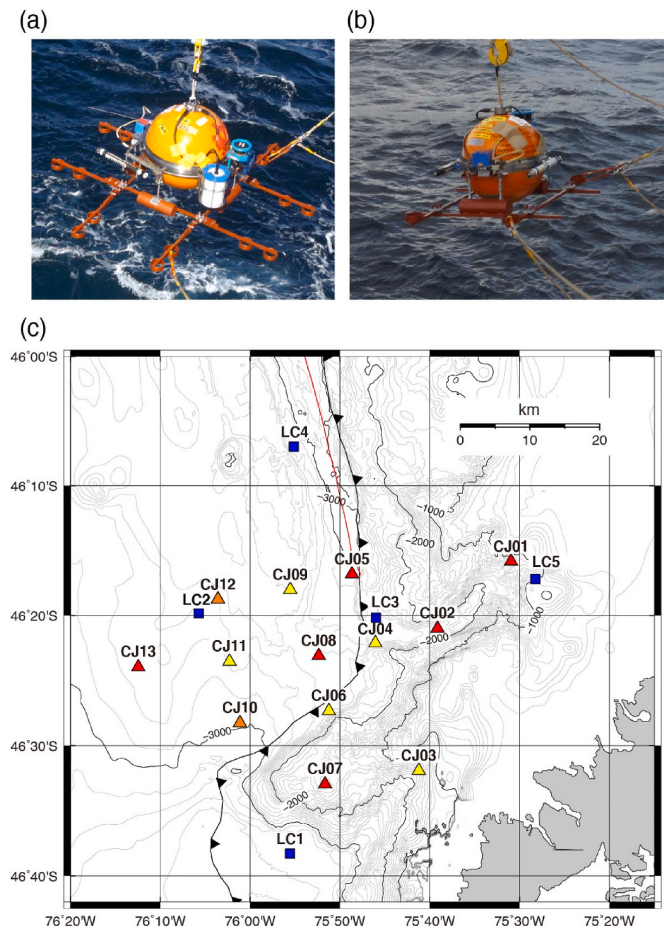


Fig. 2. (a and b) Photographic images of (a) the BBOBSs (red and orange triangles) and (b) the LTOBSs (blue squares and yellow triangles); (c) their distribution and site names. LC: first OBS array observation (Mar. 2009–Feb. 2010), CJ: second OBS array observation (Jan. 2019–Jan. 2021).

research cruise MR18-06 Leg 2 by R/V Mirai, which was operated by the Japan Agency for Marine-Earth Science and Technology (details are available in the [JAMSTEC Cruise report](#)). Once the OBSs had settled onto the seafloor, the recording was started manually using the acoustic transponder system. The recording end time for each OBS was preset as February 1, 2021. However, the recovery of the OBS array was conducted using the Chilean Navy's patrol vessel "Cirujano Videla" between January 25 and January 31, 2021 under the COVID-19 situation. As all OBSs were still in the recording state, the recordings were stopped manually using the acoustic transponder system before releasing the anchor. While all 13 OBSs came up to the sea surface, the BBOBS at the CJ05 site was unfortunately lost under the bad sea conditions in the dark. Thus, 12 OBSs (7 BBOBSs and 5 LTOBSs) were successfully recovered with full of data for the 2-year period.

2.2. Data quality

After recovery, a data quality check was performed, along with the OBS time correction and data format conversion, for distributing the data. As shown in [Table S1](#), most of OBSs had a clock drift of less than a few seconds between deployment and recovery. The maximum clock drift was -15.44 s at site CJ11, which is equivalent to approximately -0.25 ppm and is still within the internal clock specification of the data recorder. As the stability of the OBS time during the observation was already investigated by [Isse et al. \(2014\)](#), the correction for clock drift in the present work was made under the assumption that it is linear during the observational period.

Several problems did occur in some OBSs. Firstly, two LTOBSs (at CJ04 and CJ06) experienced an unexpected loss of sensor power in March 2020. However, the circuit design of the LE-3Dlite sensor was still able to output weak signals that could identify the arrival phases of many large-amplitude events. In addition, three BBOBSs (at CJ01, CJ10 and CJ12) showed bit errors in a single one-day data file at each of their industrial SD-XC cards. However, as the data format is well documented, these errors were manually edited to recover complete or continuous data with only small jumps in waveforms. No errors existed in any other data files for the 12 OBSs. The data were thoroughly readable through the time correction process, which also checked the data structure and the correct ordering of the time stamps.

For the BBOBSs, noise models were calculated to obtain an averaged power spectrum density for the entire 2-year observation period, except for time windows containing events that were reported in the PDE and the Harvard CMT Catalog. The calculation of the noise model is detailed by the [Incorporated Research Institutions for Seismology \(IRIS\) \(1994\)](#). For example, the noise models for sites CJ01 and CJ12 are presented in [Fig. 3ab](#). These sites were at different water depths of 1394 m and 2738 m, respectively. The general features of these two noise models are comparable to those of previously obtained noise models at other seafloors in the western Pacific. For instance, the vertical components of the noise levels are between the new low noise model (NLNM; [Peterson, 1993](#)) and the new high noise model (NHNM), and the horizontal components are above the NHNM. The higher horizontal noise level in CJ01 could be due to the higher-speed bottom current at the shallower depth and the topography of the land slope. Although CJ12 and CJ01 were separated by only 40 km, peaks were observed in the vertical components of their infra-gravity waves at around 50–100 s, with shifts of 75 s and 65 s, respectively, in accordance with the difference in depth. Although the mechanism is not yet well understood, strong and sharp peaks were observed in the short-period (0.1–1 s) horizontal component of CJ01 and are often seen in the data from many Japanese and USA OBSs ([OBS-IP report](#)). However, similar peaks were not observed in CJ12. Additionally, noise models of two LTOBSs are presented in [Fig. 3cd](#), for CJ03 and CJ11 whose water depths are 1828 m and 2835 m, respectively. Due to the performance of the 1 Hz sensor, the data of LTOBSs shows large noise levels at periods greater than 10 s. The same sharp peaks at short-periods are recognized also.

3. Methods and results

3.1. Station correction and event detection

As seen in [Fig. 1](#), the seafloor topography in the OBS array location is not simple, and significant variations in water depth are observed among the individual OBS sites. Hence, in the absence of huge amounts of data for precisely resolving and modeling the 3-D velocity structure, it was essential to introduce a station correction term into the traveltime data during seismic analysis, especially when a 1-D velocity structure model was being used for the hypocenter determination. Specifically, corrections were required both for the variations in water depth among the OBS sites and the existence of a soft sediment layer with slow S-wave velocity at the seafloor surface, which leads to a velocity offset in the 1-D velocity structure model beneath each OBS site ([Shiobara et al., 2010](#)).

Firstly, to estimate the initial station correction, the P to S converted phase (PS phase) at the boundary of the sediment and the basement was used. Seismograms for local earthquakes are shown in [Fig. S1](#); these were recorded at CJ11. Corrections for the P and S phase arrivals were calculated with several $T_{PS} - T_p$ data sets, where T_{PS} and T_p are the observed arrival times of the PS and the P phase, respectively, as given in Eq. (1):

$$T_{PS} - T_p = h (1/V_s - 1/V_p) \quad (1)$$

where h is the thickness of the sediment, and V_p and V_s are the P and S

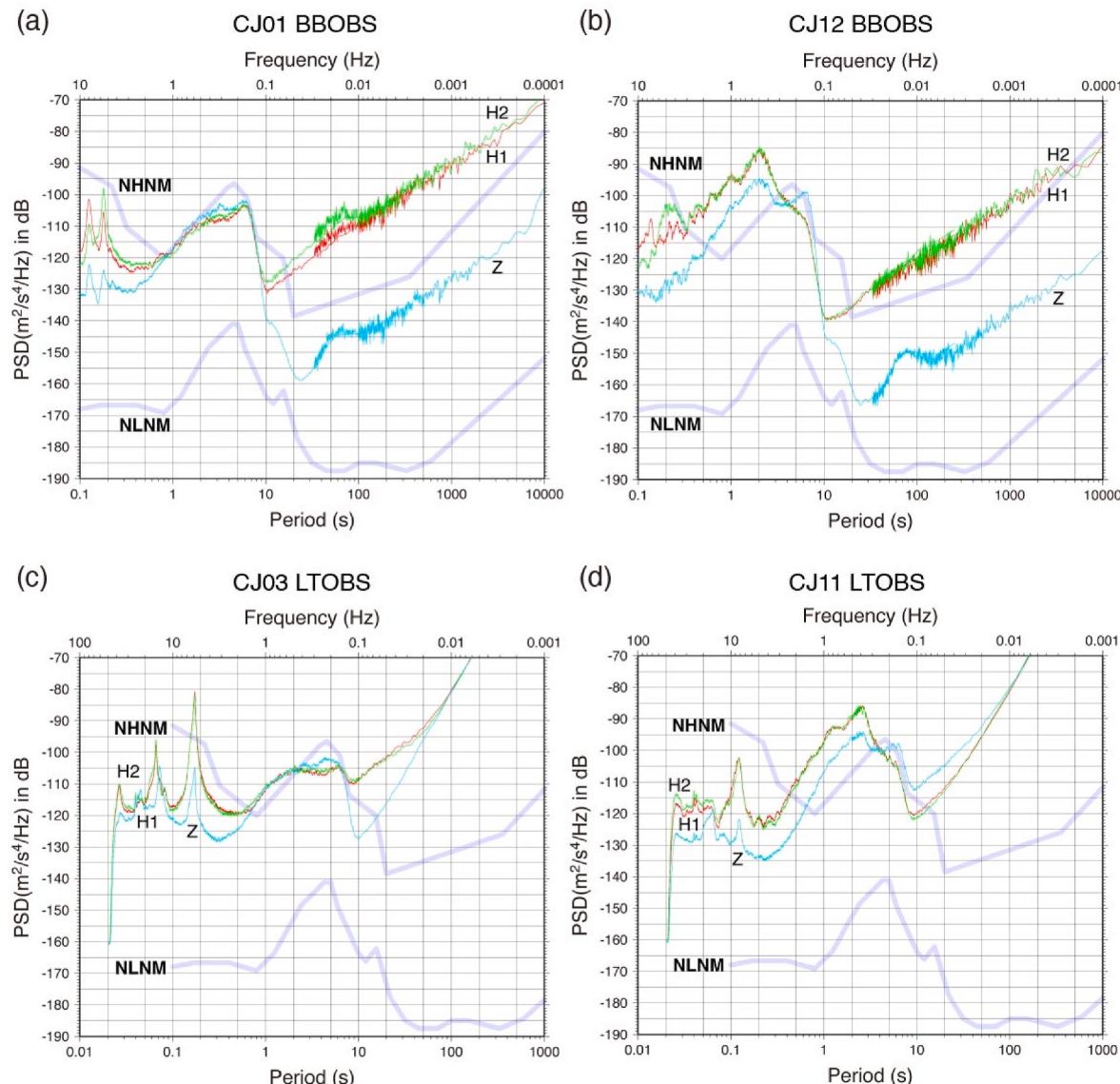


Fig. 3. The BBOBS and LTOBS noise models of CJ01 (a), CJ12 (b), CJ03 (c), and CJ11 (d). Here, the thick purple lines are the NHNM and NLNM according to Peterson (1993), and Z, H1, and H2 correspond to the respective UD, NS, and EW signals of the CMG-3T sensor for BBOBS and LE-3Dlite sensor for LTOBS. The horizontal axes in (c) and (d) are shifted toward short periods for the 1 Hz sensor used in the LTOBS.

wave velocities of the sediment, respectively.

Then, the correction terms dTp and dTs for the P and S arrivals are expressed as Eqns. (2) and (3), respectively:

$$dT_p = h (1/V_p - 1/V_p') \quad (2)$$

$$dT_s = h (1/V_s - 1/V_s') \quad (3)$$

where V_p' and V_s' are the respective P and S wave velocities in the shallow part of the 1-D velocity structure model.

The above equations can be rearranged to give Eq. (4):

$$h = (V_p V_s) (T_p - T_s) / (V_p - V_s) \quad (4)$$

A 1-D velocity model was then constructed based on the crustal structure around the trench axis at the latitude of 47.5°S, which was obtained by a seismic survey (Maksymowicz et al., 2012), as shown in Fig. S2. Here, V_p' is 2.7 km/s at depths shallower than approximately 5 km, and a V_p/V_s of 1.73 was assumed at all depths.

The observed arrival delays between the P and PS phases, and the P and S corrections for each OBS, in the 2009–2010 observational data are

summarized in Table S2, and those in the 2019–2021 observational data are summarized in Table S3. Here, the sediment velocities V_p and V_s are assumed to be 2.7 km/s and 1.2 km/s, respectively, and V_p/V_s is assumed to be 2.1, with reference to the tomographic study in the offshore region of central Chile (Hicks et al., 2014).

Next, the detection of local earthquake events was carried out using all the OBS data for the period 2019–2021. The vertical component data of each station was re-sampled at 25 Hz throughout the long observation period for quick data processing. The amplitudes of the re-sampled data were then used to detect changes in the ratio of the short time average (STA) to long time average (LTA), based on the root-mean-square (RMS) values of 1 s time windows for the STA, while the LTA windows were set to 120 s. If the STA/LTA ratio exceeded 2.0 for a period of longer than 10 s, the start time of the STA time window was regarded as corresponding empirically to a suspicious signal. Then, among all the suspicious signals, those detected at more than 4 stations separated within 20 s of each other were listed as possible events. The individual possible event data were then extracted from the continuous OBS data.

For the 2019–2021 OBS data, 3365 possible events were detected, including three $M > 4$ earthquakes occurring near the CTJ; these were

also detected by the GCMT and PDE catalogues. When the same process was performed for the 2009–2010 OBS data, suspicious signals were detected at more than 3 stations separated within 60 s of each other, and were listed as possible events. In all, 501 possible events were detected for the OBS data of the 5 LTOBSs.

3.2. Hypocenters

The manual picking of P and S phase onsets, and the determination of the hypocenters, were performed using the WIN system (Urabe and Tsukada, 1992), which includes both an interactive GUI phase picking tool and a hypocenter determination program, hypoMH (Hirata and Matsu'ura, 1987). Example of seismic record for a local earthquake is shown in Fig. S3. During phase picking, the 1-D velocity structure model shown in Fig. S2 was assumed, the phase reading errors were manually defined for each arrival, and the polarities of the P-wave first motion were recorded to estimate the focal mechanism. Not all signals marked as possible events contained identifiable seismic phases with clear onset times, and therefore the amount of picked events was fewer than the number of event triggers. After picking all locatable events, the station correction terms were iteratively modified, so as to compensate for the travel time residuals (O–C) for the P and S arrival phases of earthquakes at each station, in order to refine the hypocenter determination. As a result, 133 events were located between 2009 and 2010, and 2080 events were located between 2019 and 2021. The final station corrections (SC) and the RMS values of the O–Cs are given in Tables S2 and S3. The difference between the initial and final RMS values of the O–Cs for the P and S phases, for events in these two array observations, are shown in Fig. 4.

The resultant hypocenter distributions of the two array observations are presented in Fig. 5, where 0 km corresponds to the sea surface. Here, those earthquakes having small location errors, of less than 1 km in the horizontal direction and less than 2 km in the depth direction, are represented by red outlines around the circles. These are considered in the

remaining discussion as highly reliable earthquakes. The number of these earthquakes is 81 in the 2009–2010 observation, and 1947 in the 2019–2021 observation. In the latter case, half of the events (approximately 1000 earthquakes) occurred during only one month, between the middle of December 2020 and the end of the observational period in January 2021, as shown in Fig. 6.

In Fig. 5, seismic activities are identified along the Chile Ridge and the DFZ in both array observations, although the DFZ is outside of the OBS arrays and, hence, the earthquakes there have large location errors. Some earthquakes have been determined at depths shallower than 0 km. Most of them also have large location errors because they are located away from the center of the OBS arrays. No earthquakes were observed along the Taitao Fracture Zone (TFZ), thereby suggesting that this past transform fault is currently inactive. A clear seismicity gap is identified at 46.4°S (46° 25'S) in the second observation results (black arrows, Fig. 5b).

3.3. Magnitudes

Although the WIN system includes an interactive magnitude estimation function, we attempted to automatically estimate the earthquake magnitude independently after the phase picking process. The main reason for this is the existence of episodic high amplitude micro-seism signals, which may cause the WIN system to overestimate the amplitude. The magnitude estimation used herein is based on Watanabe's formula (Watanabe, 1971) using the maximum amplitude of the vertical component ground velocity signal empirically. For earthquakes shallower than 60 km, the magnitude value based on Watanabe's formula roughly corresponds to M_w for magnitudes of 5–7; for magnitudes smaller than 5, the comparison was not made because the value of M_w had not been frequently determined (Watanabe, 1971; Katsumata, 1996). We extrapolated the relationship between M_w and the Watanabe's value for magnitudes smaller than 5, because these magnitude values for the three $M > 4$ earthquakes are generally matched, as we will

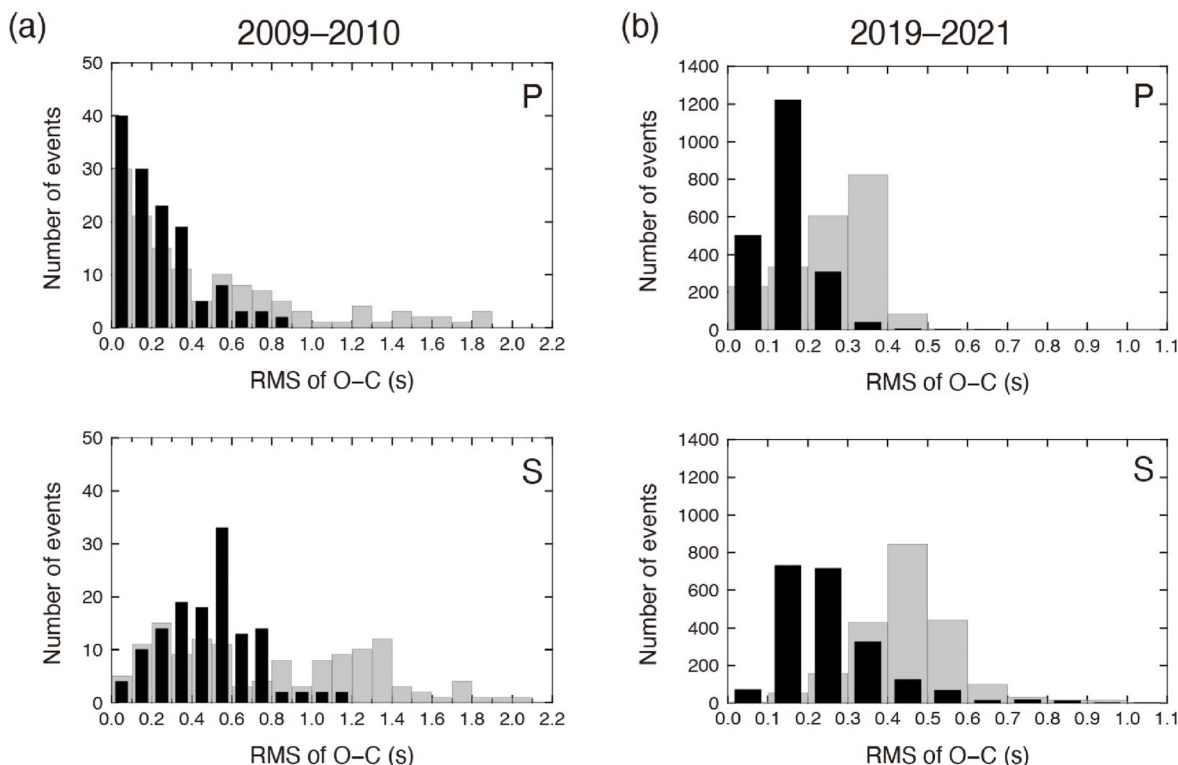


Fig. 4. Histograms showing the difference between the initial (gray) and final (black) RMS values of the travel time residuals (O–C) for the P phases (top panels) and S phases (bottom panels) for events in the observational data between (a) 2009 and 2010, and (b) 2019 and 2021.

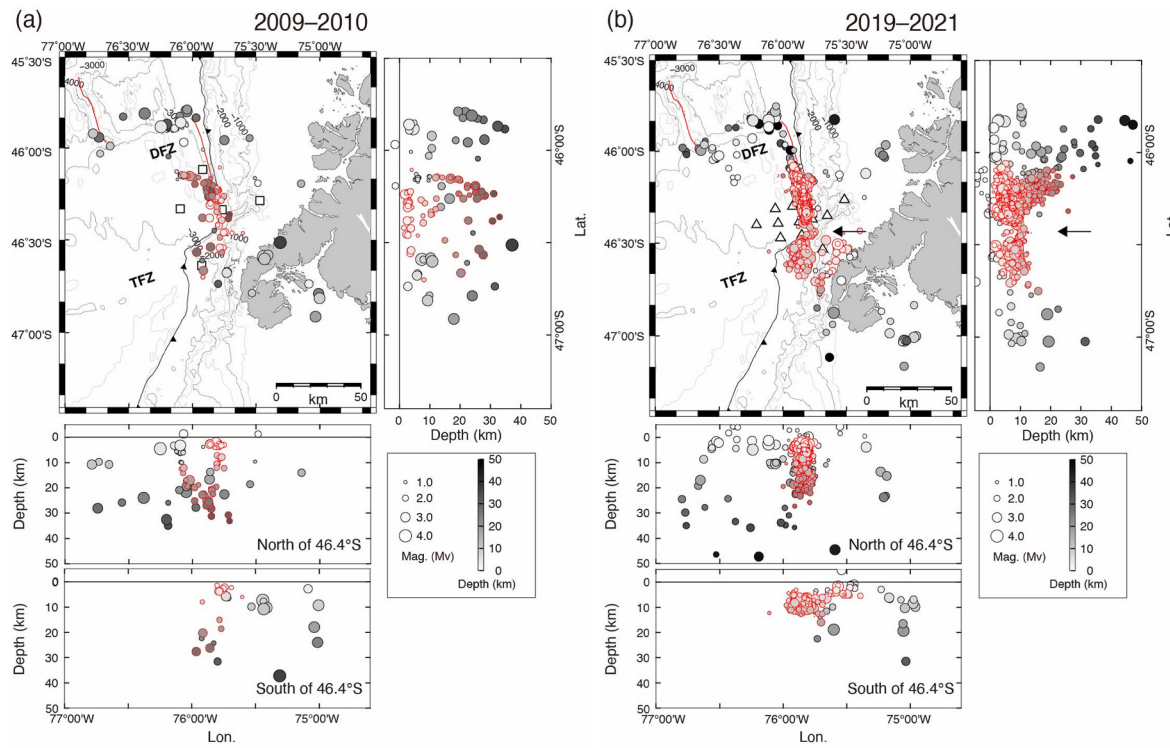


Fig. 5. The hypocenter distributions of (a) the 2009–2010 observations, and (b) the 2019–2021 observations. Here, the size and color of the circles represent the magnitude (Mv) and focal depth of the earthquake. The circles that are outlined in red represent the events with small location errors. The lower and right-hand charts show the E–W and N–S vertical sections, respectively, where 0 km corresponds to the sea surface. E–W vertical sections show the hypocenter distributions, north and south of the seismicity gap (46.4°S). The squares and triangles indicate the OBS locations, and the black arrow indicates the location of the seismicity gap.

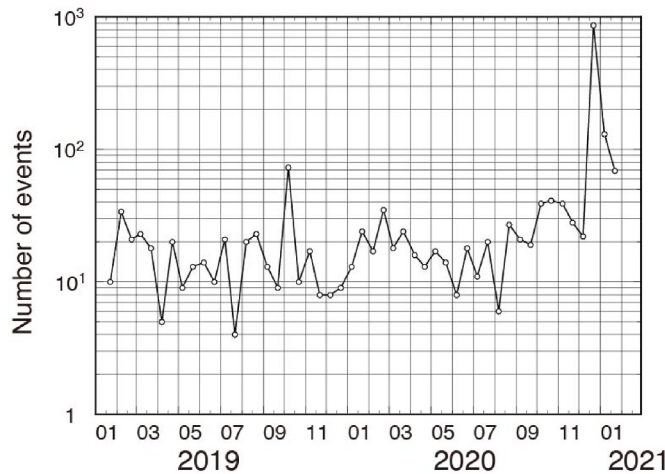


Fig. 6. The distribution of the number of events with small location errors between 2019 and 2021. The total number of each half month is plotted (i.e., the bin size is a half month). The vertical axis is in the logarithmic scale.

discuss later.

The same parameters were used for all earthquakes except for the three $M > 4$ ones. First, event records were chosen only if both the P and S phases were picked at the same site. Then, after applying a 2–10 Hz band-pass filter to the data in order to avoid the high amplitude of micro seismic noise, the maximum amplitude was sought between the onset of the P phase and 2 s after the onset of the S phase. The event magnitude was then determined by averaging the individual values at the sites. For the three $M > 4$ earthquakes, the band-pass-filtering parameter was changed to 0.5–10 Hz to cover the corner frequency, and all the P phases

used to measure the maximum amplitude were not saturated. We refer to the earthquake magnitude determined by the procedure above as “Mv” in this paper.

The magnitude of each event is indicated by the size of the corresponding circle in Fig. 5. The magnitudes range from 0.7 to 4.0 in the first array observation (Fig. 5a), and from –0.3 to 5.0 in the second array observation (Fig. 5b). In both array observations, earthquakes that occurred far from the OBS array, i.e., along the DFZ and near to, or on, the Taitao Peninsula, were detectable because of their large magnitudes. The magnitude distributions for the two observation periods are plotted in Fig. 7a. Here, the b-values are estimated from the first-order regression curve for the linear part of the data, as 0.78 for the 2009–2010 period using all events and 0.84 for the 2019–2021 period using events excluding the three $M > 4$ earthquakes that might cause bias to this estimation. Fig. 7b shows the magnitude distributions for the period 2019–2021, excluding events between December 24, 2020 and January 4, 2021 in order to eliminate the effect of $M > 4$ earthquakes, and examines the background seismicity. The b-value is estimated to be 0.94. The b-value for the period 2019–2021 is higher than that for the period 2009–2010 (0.78).

3.4. Focal mechanisms

To understand the tectonic conditions around the CTJ, the focal mechanisms of the earthquakes occurring between 2019 and 2021 were modeled. Out of the 1947 events with small location errors, 185 events with vertical component polarity readings of more than 10 sites were analyzed using the FOCMEC software (Snoke, 2003). The number of inconsistent polarity data was at most 1 out of the total polarity data set. The number of total polarity data was between 10 and 12 (i.e., at most the number of recovered OBSs). Fig. S4 shows triangle diagrams for all the focal mechanisms. Following the criteria of Frohlich (1992), the

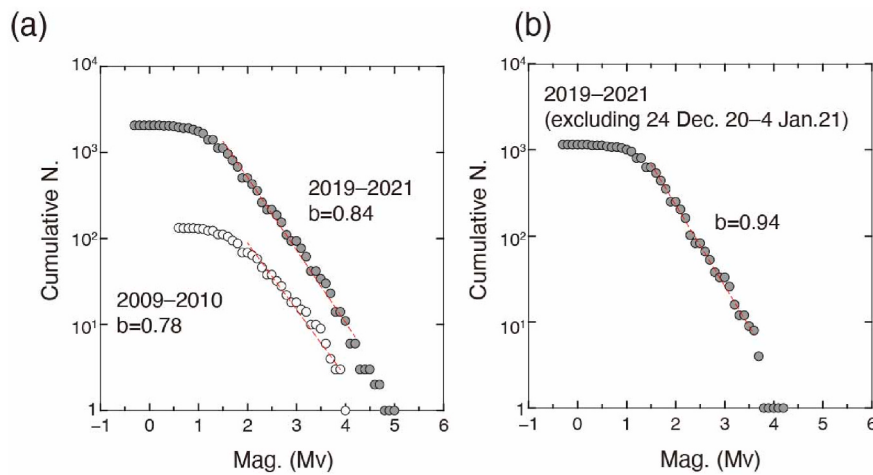


Fig. 7. The magnitude (Mv) distributions and b-values for two observations (a), and the 2019–2021 observation excluding the period from December 24, 2020 to January 4, 2021 (b). Vertical axes are in the logarithmic scale.

focal mechanisms of 41 earthquakes were classified as normal faulting, 79 as strike-slip faulting, and 63 as reverse faulting. The remaining two earthquakes were not categorized into any of these types. The resulting 183 solutions are presented in Fig. 8. Here, different focal mechanisms are recognized to the north and south of the seismicity gap at 46.4°S. In the northern area, all three faulting types are observed, with strike-slip faulting earthquakes being the most numerous, and normal faulting earthquakes being the most widely distributed. A close-up map of focal mechanisms in the northern area is shown in Fig. S5. By contrast, the southern area is dominated by reverse faulting, and shows fewer strike-slip and normal faulting earthquakes.

The temporal sequence of seismic activity according to faulting type is shown in Fig. 8c and d, along with the events with small location errors (open gray circles). Here, more than 10 normal faulting earthquakes are seen to have periodically occurred in the northern area, while numerous earthquakes of all three types occurred after the three $M > 4$ earthquakes on December 26, 2020. This period range, between December 24, 2020 and January 5, 2021, is shown in Fig. 8d to make clear the event sequence of the three $M > 4$ earthquakes and their fore- and aftershocks. Also shown is the spatial concentration of normal fault type earthquakes. Meanwhile, reverse faulting earthquakes are seen to have occurred periodically in the southern area.

The compressive stress axes of the three faulting types at the epicenter positions are shown in Fig. 9. Although there are some directional variations, the minimum compressive axes (T-axes) of the normal faulting and strike-slip earthquakes, and the maximum compressive axes (P-axes) of the reverse faulting earthquakes, are approximately E–W.

4. Discussion

4.1. Comparison of two OBS array observations

Two OBS array observations with different spacings, numbers of stations, and observation periods were performed, and the local earthquakes were located using similar parameters. The largest difference in seismic activity between the two observation periods was the occurrence of three $M > 4$ earthquakes on December 26, 2020. These were followed by approximately 1000 aftershocks. In terms of the total number of events with small location errors, the second observation period was found to include 1947 events, which was more than 20 times as many as in the first period (81 events). The number of earthquakes during each observational period was then compared with the normal background seismicity, excluding December 2020 to January 2021 in order to

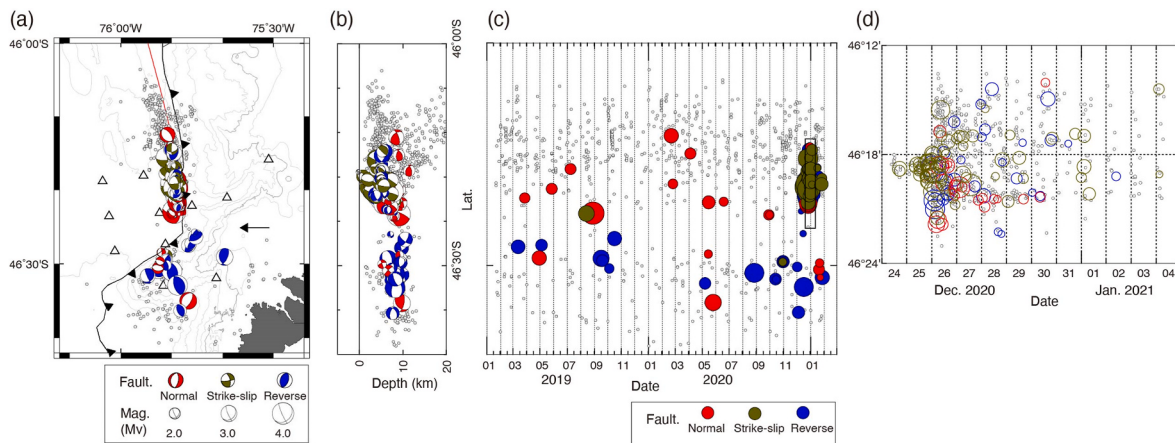


Fig. 8. The focal mechanism solutions (a), N–S vertical section (b), and temporal sequence (c) for the 2019–2021 data, and the closeup of (c) in the rectangle area (d), where the small dots represent the hypocenters of events with small location errors. In (a), the red, dark green, and blue beach balls correspond to normal, strike-slip, and reverse-faulting earthquakes, respectively, and the black arrow indicates the location of the seismicity gap. The focal mechanisms are indicated in the lower hemisphere projections, where the size of the focal mechanism indicates the earthquake magnitude (Mv). In (b), 0 km corresponds to the sea surface. In (c) and (d), the colors and sizes of the circles correspond to the faulting type and the magnitude shown in (a), respectively.

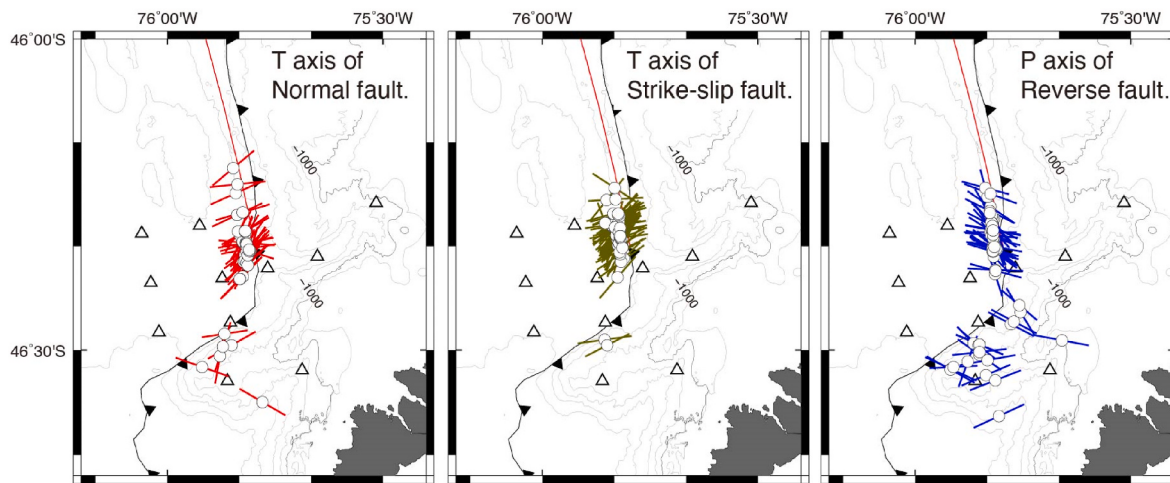


Fig. 9. The minimum compressive stress axes in the normal faulting (left) and strike-slip faulting (middle) earthquakes, and the maximum compressive stress axes in the reverse faulting (right) earthquakes.

eliminate the effects of the $M > 4$ earthquakes (Fig. 6). Thus, approximately 1000 events with small location errors occurred during two years within the second observational period, which corresponds to 500 per year. This was 5 times as many such events as in the first observation period. This increase in the number of detected earthquakes might be because the second OBS array was more capable of locating the earthquakes, or because the background seismicity was genuinely higher during the second observational period, or both.

The improved earthquake detection capability of the second OBS array is mainly due to the increase in the number of OBSs and the shorter distances between the stations. The intensive coverage area of the observations is also important for investigating the seismicity of the region. Compared to the first OBS array, the OBSs in the second observation were more concentrated at the southern CTJ region (Fig. 2), thereby facilitating the detection of the seismicity gap at 46.4°S . This seismicity gap was revealed by the existence of large numbers of earthquakes to the north and south of the CTJ region, but few earthquakes close to the CTJ (Fig. 5b). However, the first OBS array detected only a small number of earthquakes in the southern CTJ region (Fig. 5a), even though earthquakes probably were occurring there regularly during the first observation period, as discussed in Section 4.3 below. Thus, the first OBS array failed to identify the seismicity gap.

4.2. $M > 4$ earthquakes on Dec. 26, 2020

The three $M > 4$ events that occurred near the CTJ on December 26, 2020 were the only events whose magnitude and Centroid Moment Tensor (CMT) solutions were determined from the global data during the two observation periods. These seem to be rare events, because most of earthquakes that were detected by the global networks were located along the DFZ. The hypocenter locations, magnitudes, and focal mechanisms of the three $M > 4$ earthquakes are summarized in Table 1, where events A and B were reported by the GCMT (Mw), and events B and C were reported by the PDE (mb). In this study, the magnitudes of the three events were estimated to be Mv 4.6–5.0, which are closely comparable to those determined from the global data. In detail, the presently estimated magnitudes of events A and C are larger than those of the global data by 0.2–0.3, while that of event B is 0.1 lower than the GCMT and larger than the PDE. Considering the differences in data acquisition and analysis methods (waveform inversion for the CMT solutions or the maximum amplitude of the body waves in the global data versus the maximum amplitude of the vertical component in this study), we believe that the magnitude determination process used in this study provides reasonable results for the estimation of earthquake magnitudes.

Table 1
Summary of $M > 4$ earthquakes occurred on Dec. 26, 2020.

Event	GCMT		PDE (USGS)		This study		
	A	B	B	C	A	B	C
Time (hh:mm)	01:47	02:19	02:19	02:23	01:47	02:19	02:23
Lat. ($^{\circ}\text{S}$)	46.25	46.29	46.08	46.32	46.32	46.32	46.32
Lon. ($^{\circ}\text{W}$)	75.98	75.91	75.91	76.10	75.82	75.82	75.83
Dep. (km)	20	18	10	10	3.6	4.0	2.9
Fault. Type	Strike-slip	Strike-slip	–	–	Strike-slip	Other	Strike-slip
Fault plane 1	352/68/–18	350/66/–22	–	–	170/85/2	338/30/9	342/83/–13
Fault plane 2	90/73/–156	90/70/–154	–	–	80/88/175	241/86/120	74/77/–172
Magnitude	Mw 4.8	Mw 4.9	mb 4.7	mb 4.3	Mv 5.0	Mv 4.8	Mv 4.6

Fault planes 1 and 2: Strike/Dip/rake (slip).

A comparison of the hypocenters is presented in Fig. 10a. Here, the GCMT and PDE data give widely separated locations for each event, but the three hypocenters were almost identical (46.3°S , 75.8°W) in this study, with a high level of accuracy due to the nearby OBS array. Indeed, the location errors of the three events were 0.1 km in both the horizontal and depth directions. Thus, these three events are thought to have occurred close together at the same fault plane, at a shallow depth of 3–4 km. The epicenters were located approximately 10 km north of the seismicity gap.

The focal mechanism solutions and distribution of polarities obtained in the present study are shown in Fig. 10b. Events A and C are strike-slip faulting earthquakes, whereas event B is not categorized into any of the three faulting types, in accordance with the criteria of Frohlich (1992). However, the three earthquakes are regarded as having similar focal mechanisms of the strike-slip faulting type because all three occurred close together in terms of both location and time. The GCMT also estimated the CMT solutions of events A and B to be strike-slip faulting, with approximately N-S or E-W strike directions. We propose that all three $M > 4$ earthquakes are more likely to be right-lateral strike-slip faulting earthquakes, similar to those occurring along the DFZ. Here, a type of local transform fault with an E-W strike direction is possibly formed around the CTJ due to the active ridge subduction, and the three $M > 4$ earthquakes would have occurred along this local transform fault. It is unlikely that active fault planes with N-S strike

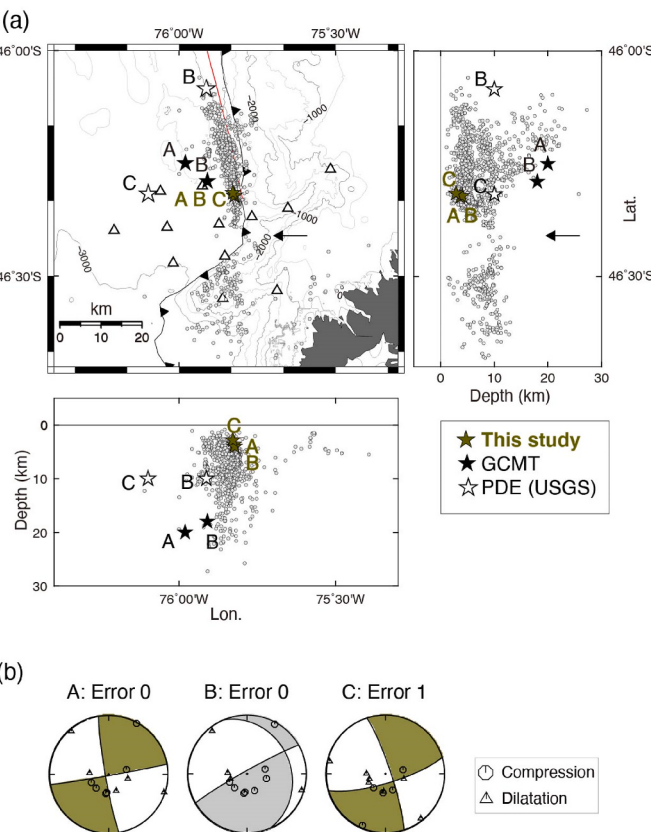


Fig. 10. A comparison of the hypocenters (a), and focal mechanism solutions (b) for the three $M > 4$ earthquakes that occurred on December 26, 2020. In (a), the dark green, black, and white stars correspond to the hypocenters obtained by the present study, the GCMT, and the PDE, respectively, the small dots show the hypocenters of events with small location errors between 2019 and 2021, and the black arrow indicates the location of the seismicity gap.

direction were formed in the studied area, because the relative plate motions of both the Antarctic and Nazca plates are almost E–W in direction (E–W and ENE–WSW, respectively; DeMets et al., 2010).

4.3. Seismic activities north and south of the seismicity gap

In the present study, distinct seismic activities were observed to the north and south of a clear seismicity gap at 46.4°S . To the north, where the Chile Ridge is located, several normal faulting earthquakes periodically occurred along the Ridge at shallow depths of approximately 10 km beneath the sea surface, as shown in Fig. 8. Taking account of the 3-km seafloor depths in this region, it corresponds to a depth of approximately 7 km below the seafloor. Based on this result, we consider that these normal faulting earthquakes are probably associated with the continuous ridge opening. Based on numerical experiments and the results of observational data in several ridge regions, Morgan and Chen (1993) proposed that the lower depth limit of earthquakes associated with the ridge opening depends mainly on the thermal conditions and derived the relationship between the earthquake depth and the spreading rate of the ridge. In their study, the lower depth limit was estimated to be approximately 6 km beneath the seafloor, at the current half spreading rate of the Chile Ridge (26.5 mm/yr; Tebbens et al., 1997). This depth is reasonably consistent with the value obtained in the present study (7 km).

After December 2020, numerous earthquakes with normal, strike-slip, and reverse faulting were observed along the ridge axis to the north of the seismicity gap (Fig. 8). These represent aftershocks of the $M > 4$ earthquakes, and were concentrated at depths shallower than 5 km.

Their epicenters were spread across a length of 20 km in the N–S direction, which was slightly narrower than the distribution of normal faulting earthquakes associated with the continuous ridge opening. The normal faulting aftershocks were possibly located along the ridge, while the strike-slip and reverse faulting aftershocks might reflect the complex stress field affected by the active ridge subduction. A fracture zone may exist along the shallower portion of the ridge (less than 5 km), extending 20 km in the N–S direction. It includes a number of small fault planes with E–W strike direction, because the T-axes of the strike-slip faulting aftershocks (middle panel, Fig. 9) and the P-axes of the reverse faulting aftershocks (right-hand panel, Fig. 9) were both oriented roughly E–W. The major fault plane within the fracture zone may correspond to the local transform fault proposed in Section 4.2.

South of the seismicity gap, where the Chile Ridge has already been subducted, reverse faulting earthquakes were predominant and occur periodically. Their P-axes were oriented roughly E–W, i.e., parallel to the subduction direction of the Antarctic Plate (right-hand panel, Fig. 9). These earthquakes were probably associated with the Antarctic plate subduction and are occurring regularly.

5. Conclusions

To investigate crustal activities and seismic structures, two OBS array observations were conducted in the vicinity of the CTJ, and the hypocenter distributions, earthquake magnitudes, and focal mechanism solutions of local earthquakes were determined. The period of the first OBS array observation was between 2009 and 2010, and the second one was between January 2019 and January 2021. Whereas the first observation had a site spacing of more than 20 km, the spacing for the second observation was set at about 10 km, thereby improving the capability and accuracy of the hypocenter determination.

In total, 133 hypocenters with M_v of 0.7–4.0 were identified between 2009 and 2010, and 2080 hypocenters with M_v of –0.3 to 5.0 were identified between 2019 and 2021. High seismic activities were observed along the Chile Ridge and the DFZ in both observations, whereas no earthquakes were observed along the TFZ.

A clear seismicity gap was identified at 46.4°S in the hypocenter distribution between 2019 and 2021, with distinct faulting types occurring to the north and south thereof. Thus, to the north of the seismicity gap, normal faulting earthquakes occur periodically along the Chile Ridge, and are associated with the continuous ridge opening. To the south of the seismicity gap, where the Chile Ridge has already been subducted, reverse faulting earthquakes associated with the Antarctic plate subduction are predominant and occur regularly.

In addition, three $M > 4$ earthquakes occurred on December 26, 2020 at almost same location, approximately 10 km north of the seismicity gap. These were possibly right-lateral strike-slip faulting earthquakes. We suggest that these earthquakes occurred along that a putative local transform fault with an E–W strike direction near the CTJ. Numerous strike-slip and reverse faulting aftershocks were also observed, and were distributed across a length of 20 km in the N–S direction. This aftershock activity reflects the complex stress field along the ridge under active subduction.

The OBS array observations described herein revealed the details of seismic activities around the CTJ, which could only be obtained from offshore observations far from the land network. Nevertheless, there are uninterpreted issues remaining, including the existence of the seismicity gap and its relation to the active ridge subduction. Moreover, further studies on the seismic velocity structure, especially the underlying 3-D structure and the thermal and fluid conditions around the CTJ, are needed in order to better understand of the CTJ region. Hence, we intend to perform several further studies to investigate the seismic structure described in the introduction section. In particular, the BBOBS data obtained during the second OBS array observation has enabled the investigation of seismic structure with broad-band data coverage.

CRediT authorship contribution statement

Aki Ito: Writing – original draft. **Hajime Shiobara:** Writing – original draft. **Matthew Miller:** Writing – review & editing. **Hiroko Sugioka:** Writing – review & editing. **Javier Ojeda:** Writing – review & editing. **Carlos Tassara:** Writing – review & editing. **Masanao Shino-hara:** Investigation. **Masataka Kinoshita:** Writing – review & editing. **Hikaru Iwamori:** Project administration.

Declaration of competing interest

The authors declare that they have no known competing financial interests or personal relationships that could have appeared to influence the work reported in this paper.

Data availability

The data will be available from the Ocean Hemisphere Project Data Management Center, Earthquake Research Institute, University of Tokyo.

Acknowledgements

We thank the captains and crews of R/V Mirai and the Chilean Navy's General service patrol boat Cirujano Videla for their help during the OBS work, and the Chile government office SHOA (Servicio Hidrográfico y Oceanográfico de la Armada de Chile) for the helpful cooperation. We greatly appreciate Dr. Takashi Iida of the Earthquake Research Institute, the University of Tokyo, for supporting us in the magnitude determination, and Dr. Nobukazu Seama and Yuko Kondo of Kobe University, and Drs. Toshiya Fujiwara and Masayuki Obayashi at JAMSTEC, for their useful advice on the tectonic setting and seismicity at the ridge region. Drs. Tomoaki Yamada and Takehi Isse of the Earthquake Research Institute, the University of Tokyo, participated in the first OBS observation. We also thank the Geophysics Masters degree program at the University of Concepcion, Sergio Ruiz, Roberto Riquelme and Freddy Echeverria for their contribution to the logistics of the OBS recovery operation undertaken during COVID-19 restrictions. JO acknowledges support from the Agencia Nacional de Investigación y Desarrollo (Scholarship ANID-PFCHA/Doctorado Nacional/2020–21200903). Two anonymous reviewers greatly helped to improve the manuscript. Many figures in this paper were produced using the Generic Mapping Tools (Wessel et al., 2019).

Appendix A. Supplementary data

Supplementary data to this article can be found online at <https://doi.org/10.1016/j.james.2023.104285>.

References

- Araki, E., Sugioka, H., 2009. Calibration of deep sea differential pressure gauge. *JAMSTEC Rep. Res. Dev.* 9, 141–148 (in Japanese with English abstract).
- Barrientos, S.E., Ward, S.N., 1990. The 1960 Chile earthquake: inversion for slip distribution from surface deformation. *Geophys. J. Int.* <https://doi.org/10.1111/j.1365-246X.1990.tb05673.x>.
- Breitsprecher, K., Thorkelson, D.J., 2009. Neogene kinematic history of Nazca–Antarctic–Phoenix slab windows beneath Patagonia and the Antarctic Peninsula. *Tectonophysics* 464 (1–4), 10–20. <https://doi.org/10.1016/j.tecto.2008.02.013>.
- Cande, S.C., Leslie, R.B., 1986. Late cenozoic tectonics of the southern Chile trench. *J. Geophys. Res. Solid Earth* 91, 471–496. <https://doi.org/10.1029/JB091iB01p00471>.
- Contreras-Reyes, E., Grevemeyer, I., Flueh, E.R., Scherwath, M., Heesemann, M., 2007. Alteration of the subducting oceanic lithosphere at the southern central Chile trench–outer rise. *Geochem. Geophys. Geosys.* 8 <https://doi.org/10.1029/2007GC001632>.
- Contreras-Reyes, E., Jara, J., Grevemeyer, I., Ruiz, S., Carrizo, D., 2012. Abrupt change in the dip of the subducting plate beneath north Chile. *Nat. Geosci.* 5, 342–345. <https://doi.org/10.1038/Ngeo1447>.
- DeMets, C., Gordon, R.G., Argus, D.F., 2010. Geologically current plate motions. *Geophys. J. Int.* 181, 1–80. <https://doi.org/10.1111/j.1365-246X.2009.04491.x>.
- Frohlich, C., 1992. Triangle diagrams: ternary graphs to display similarity and diversity of earthquake focal mechanisms. *Phys. Earth Planet. In.* 75, 93–198.
- Gallego, A., Russo, R.M., Comte, D., Mocanu, V., Murdie, R.E., VanDecar, J.C., 2013. Tidal modulation of continuous nonvolcanic seismic tremor in the Chile triple junction region. *Geochem. Geophys. Geosys.* 14 <https://doi.org/10.1002/ggge.20091>.
- Haberland, C., Rietbrock, A., Lange, D., Bataille, K., Dahm, T., 2009. Structure of the seismogenic zone of the southcentral Chilean margin revealed by local earthquake traveltime tomography. *J. Geophys. Res. Solid Earth* 114. <https://doi.org/10.1029/2008JB005802>.
- Hicks, S.P., Rietbrock, A., Ryder, I.M.A., Lee, C., Miller, M., 2014. Anatomy of a megathrust: the 2010 M8.8 Maule, Chile earthquake rupture zone imaged using seismic tomography. *Earth Planet Sci. Lett.* 405, 142–155. <https://doi.org/10.1016/j.epsl.2014.08.028>.
- Hirata, N., Matsuzawa, M., 1987. Maximum-likelihood estimation of hypocenter with origin time eliminated using nonlinear inversion technique. *Phys. Earth Planet. In.* 47, 50–61. [https://doi.org/10.1016/0031-9201\(87\)90066-5](https://doi.org/10.1016/0031-9201(87)90066-5).
- Husen, S., Kissling, E., Flueh, E.R., 2000. Local earthquake tomography of shallow subduction in north Chile: a combined onshore and offshore study. *J. Geophys. Res.* 105, 28183–28198. <https://doi.org/10.1029/2000JB900229>.
- Husen, S., Kissling, E., Flueh, E.R., Asch, G., 1999. Accurate hypocentre determination in the seismogenic zone of the subducting Nazca Plate in northern Chile using a combined on/offshore network. *Geophys. J. Int.* 138 (3), 687–701. <https://doi.org/10.1046/j.1365-246X.1999.00893.x>.
- Ide, S., 2012. Variety and spatial heterogeneity of tectonic tremor worldwide. *J. Geophys. Res. Solid Earth* 117. <https://doi.org/10.1029/2011JB008840>.
- Incorporated Research Institutions for Seismology (IRIS), 1994. Estimation of seismic noise. In: Federation of Digital Seismograph Networks: Station Book. IRIS Data Management System, Appendix F, Washington, DC, p. 7.
- Isse, T., Kawakatsu, H., Yoshizawa, K., Takeo, A., Shiobara, H., Sugioka, H., Ito, A., Suetsugu, D., Reymond, D., 2019. Surface wave tomography for the Pacific Ocean incorporating seafloor seismic observations and plate thermal evolution. *Earth Planet Sci. Lett.* 510, 116–130. <https://doi.org/10.1016/j.epsl.2018.12.033>.
- Isse, T., Takeo, A., Shiobara, H., 2014. Time correction and clock stability of ocean bottom seismometer using recorded seismograms. *JAMSTEC Rep. Res. Dev.* 19, 19–28 (in Japanese with English abstract).
- Iwamori, H., 2000. Thermal effects of ridge subduction and its implications for the origin of granitic batholith and paired metamorphic belts. *Earth Planet Sci. Lett.* 181, 131–144. [https://doi.org/10.1016/S0012-821X\(00\)00182-5](https://doi.org/10.1016/S0012-821X(00)00182-5).
- JAMSTEC cruise report. https://www.godac.jamstec.go.jp/cr_catalog/external/metadata/MR18-06_leg2_all/file/MR18-06_leg2_all.pdf.
- Katsumata, A., 1996. Comparison of magnitudes estimated by the Japan Meteorological Agency with moment magnitudes for intermediate and deep earthquakes. *Bull. Seismol. Soc. Am.* 86 (3), 832–842.
- Lagabrielle, Y., Bourgois, J., Dymnt, J., Pelletier, B., 2015. Lower plate deformation at the Chile Triple Junction from the paleomagnetic record (45°S–46°S). *Tectonics* 34. <https://doi.org/10.1002/2014TC003773>.
- Lagabrielle, Y., Guivel, C., Maury, R.C., Bourgois, J., Fourcade, S., Martin, H., 2000. Magmatic–tectonic effects of high thermal regime at the site of active ridge subduction: the Chile Triple Junction model. *Tectonophysics* 326, 255–268. [https://doi.org/10.1016/S0040-1951\(00\)00124-4](https://doi.org/10.1016/S0040-1951(00)00124-4).
- Lange, D., Rietbrock, A., Haberland, C., Bataille, K., Dahm, T., Tilmann, F., Flüh, E.R., 2007. Seismicity and geometry of the south Chilean subduction zone (41.5°S–43.5°S): implications for controlling parameters. *J. Geophys. Res. Solid Earth* 112. <https://doi.org/10.1029/2006GL029190>.
- Maksymowicz, A., Contreras-Reyes, E., Grevemeyer, I., Flueh, E.R., 2012. Structure and geodynamics of the post-collision zone between the Nazca–Antarctic spreading center and South America. *Earth Planet Sci. Lett.* 345/348, 27–37. <https://doi.org/10.1016/j.epsl.2012.06.023>.
- McKenzie, D.P., 1967. Some remarks on the heat flow and gravity anomalies. *J. Geophys. Res.* 72, 6261–6273. <https://doi.org/10.1029/JZ072i024p06261>.
- Moreno, M.S., Bolte, J., Klotz, J., Melnick, D., 2009. Impact of megathrust geometry on inversion of coseismic slip from geodetic data: application to the 1960 Chile earthquake. *Geophys. Res. Lett.* <https://doi.org/10.1029/2009GL039276>.
- Morgan, J., Chen, Y., 1993. Dependence of ridge-axis morphology on magma supply and spreading rate. *Nature* 364, 706–708. <https://doi.org/10.1038/364706a0>.
- OBS-IP report. Woods hole oceanographic institution, <https://obsic.whoi.edu/data/6hz-noise/>.
- Parker, R.L., Oldenburg, D.W., 1973. Thermal model of ocean ridges. *Nat. Phys. Sci. (Lond.)* 242, 137–139. <https://doi.org/10.1038/physci242137a0>.
- Peterson, J., 1993. Observations and Modelling of Seismic Background Noise. USGS Open File Report, pp. 93–322.
- Sáez, M., Ruiz, R., Ide, S., Sugioka, H., 2019. Triple Junction: shallow nonvolcanic tremor activity and potential repeating earthquakes in the Chile triple junction: seismic evidence of the subduction of the active Nazca–Antarctic spreading center. *Seismol. Res. Lett.* 90 <https://doi.org/10.1785/0220180394>.
- Scherwath, M., Contreras-Reyes, E., Flueh, E.R., Grevemeyer, I., Krabbenhoft, A., Papenberg, C., Petersen, J., Weinrebe, R.W., 2009. Deep lithospheric structures along the southern central Chile margin from wide-angle P-wave modelling. *Geophys. J. Int.* 179 <https://doi.org/10.1111/j.1365-246X.2009.04298.x>.
- Shinohara, M., Suyehiro, K., Shiobara, H., 2012. Marine seismic observation, in: CHAPTER 7.5 of Site selection, preparation, and installation of seismic stations. In: Bormann, P. (Ed.), New Manual of Seismological Observatory Practice 2 (NMSOP-2).

- IASPEI, GFZ German Research Centre for Geosciences, Potsdam. <https://doi.org/10.2312/GFZ.NMSOP-2.ch7>.
- Shinohara, M., Yamada, T., Sugioka, H., Ito, A., Miller, M., Isse, T., Bataille, K., Iwamori, H., 2010. Microearthquake Observation Around Chile Triple Junction by Using Long-Term Ocean Bottom Seismometers. abstract in. The Geochemical Society of Japan. <https://doi.org/10.14862/geochemproc.57.0.160.0> (in Japanese).
- Shiobara, H., Ito, A., Sugioka, H., Shinohara, M., Sato, T., 2021. Tilt observations at the seafloor by mobile ocean bottom seismometers. *Front. Earth Sci.* <https://doi.org/10.3389/feart.2020.599810>.
- Shiobara, H., Sugioka, H., Mochizuki, K., Oki, S., Kanazawa, T., Fukao, Y., Suyehiro, K., 2010. Double seismic zone in the North Mariana region revealed by long-term ocean bottom array observation, 2010 *Geophys. J. Int.* 183 (3), 1455–1469. <https://doi.org/10.1111/j.1365-246X.2010.04799.x>.
- Snoke, J.A., 2003. FOCMEC: FOcal MEchanism determinations. In: Lee, W.H.K., Kanamori, H., Jennings, P.C., Kisslinger, C. (Eds.), *International Handbook of Earthquake and Engineering Seismology*. Academic Press, San Diego (Chapter 85).12.
- Suetsugu, D., Shiobara, H., 2014. Broadband Ocean bottom Seismology. *Annu. Rev. Earth Planet Sci.* 42, 27–43. <https://doi.org/10.1146/annurev-earth-060313-054818>.
- Tebbens, S.F., Cande, S.C., Kovacs, L., Parra, J.C., LaBrecque, J.L., Vergara, H., 1997. The Chile ridge: a tectonic framework, 035–12,059 *J. Geophys. Res.* 102 (12). <https://doi.org/10.1029/96JB02581>.
- Tilmann, F., Grevemeyer, I., Flueh, E.R., Dahm, T., Gossler, J., 2008. Seismicity in the outer rise offshore southern Chile: indication of fluid effects in crust and mantle. *Earth Planet Sci. Lett.* 269, 41–55. <https://doi.org/10.1016/j.epsl.2008.01.044>.
- Urabe, T., Tsukada, S., 1992. WIN:A workstation program for processing waveform data from micro earthquake networks. *Prog. Abstr. Seis. Soc. Jpn.* 2, 331 (in Japanese).
- Watanabe, H., 1971. Determination of earthquake magnitude at regional distance in and near Japan. *Zishin 2 (J. Seismol. Soc. Jpn. 2nd ser.)* 24, 189–200. <https://doi.org/10.4294/zisin1948.24.3.189> (in Japanese with English abstract).
- Wessel, P., Luis, J.F., Uieda, L., Scharroo, R., Wobbe, F., Smith, W.H.F., Tian, D., 2019. The generic mapping tools version 6. *Geochem. Geophys. Geosys.* 20, 5556–5564. <https://doi.org/10.1029/2019GC008515>.